Engineering and Technology Journal
Journal homepage: https://etj.uotechnology.edu.iq

Aerodynamic characteristics evaluation of s-series airfoils

Hamzah M. Jaffar[a], Laith A. Al-Sadawi[a*], Abdulkareem A. Khudhair[a], Till Biedermann[b]

[a]Mechanical Engineering Dept., University of Technology-Iraq, Alsina'a street, 10066 Baghdad, Iraq.
[b] R&D at Pollrich GmbH, Siegen, Germany.
*Corresponding author Email:laith.a.salman@uotechnology.edu.iq

HIGHLIGHTS

- Ansys-Fluent predicts flow around thick airfoils wall at low/mid angles. High angles: lift, drag, near-wake
- The airfoil shape significantly shapes the airfoil and wake region flow
- S818, S811 airfoils performed best in crossflow while S809, S814 showed poor aerodynamics, especially at high angles

ARTICLE INFO

Handling editor: Sattar Aljabair

Keywords:
Thick airfoil
S-series airfoils
Horizontal axis wind turbine
CFD
Wind turbine

ABSTRACT

The present study utilizes the commercial software ANSYS-Fluent to explore the influence of the geometry of thick S- S-series airfoil on the near-wake region. Four different S-series airfoils, namely S809, S811, S814, and S818, were investigated at a wide range of angles of attack, which were varied from 0 degrees to 20 degrees with an increment of 2 degrees and at a Reynolds number based on chord length Re = $1x10^6$. Analysis of the resultant data revealed that the aerodynamic performance of the S811 and S818 airfoils superseded that of the S809 and S814 airfoils. To illustrate, at the critical angle of attack, S811 and S818 were observed to possess the maximum lift and minimum drag coefficients. Furthermore, in the range of attack angles between 10 and 16 degrees, these airfoils consistently demonstrated lower drag than the others tested, enhancing overall aerodynamic performance. These findings underscore the significant role played by airfoil geometry in influencing aerodynamic performance and provide insights into optimal design parameters for wind turbine blades, particularly highlighting the advantages of the S811 and S818 airfoil shapes. In addition, the effect of the unsteady structures in the near-wake zone behind the trailing was also evaluated through turbulence kinetic energy contours. The results revealed a decrease in turbulence kinetic energy when the S811 and S818 airfoils were placed in a cross-flow compared to the S809 and S814 airfoils. This indicates that the strength of the vortex shedding of these airfoils is lower than that of the S809 and S8014 airfoils.

1. Introduction

Wind power is developing faster than other renewable energy sources in the energy sector. In 2012, 285 GW of wind turbines were erected worldwide, with that amount predicted to rise to 500 GW by 2017. Wind turbine size, efficiency, and reliability have been improved while costs, complexity, and safety risks have been reduced. The blade design, which has stayed similar despite growing capacity and consumption, is one subject of inquiry. Scientists are investigating the use of various materials for wind turbine blade manufacturing in order to improve wind turbine aerodynamics, control efficiency, and reliability [1].

The aerodynamic design of wind turbine blades, which substantially impacts the amount of power that can be generated from wind, is one of the most significant concerns in the wind business. Although it may appear rational to use airfoil sections from aircraft wings, studies, and applications have demonstrated that wind turbines require particular airfoil designs that can be managed in a variety of weather circumstances. Unlike aviation airfoil sections, wind turbine airfoils require a "gentle stall" to minimize excessive energy capture losses when the wind speed is low [2]. Because the rotor blade is an essential component of wind turbines, developing airfoil sections to fulfill global energy needs is critical. Wind turbine blades comprise three sections: an airfoil's root, middle, and tip. The airfoil sections' design varies with the wind turbine's capacity. Although it does not affect torque, increasing the lift coefficient can increase thrust, reduce drag, and enhance aerodynamic efficiency [3].

In 1984, the Sun Energy Research Institute (SERI), now called the National Renewable Energy Laboratory (NREL), collaborated with Airfoils Inc. to create specialized airfoils for horizontal-axis wind turbines (HAWTs) [4]. Over a decade, they used the Eppler Airfoil Design and Analysis Code to develop nine unique airfoil families and 25 individual airfoils for use on

http://doi.org/10.30684/etj.2023.141757.1512
Received 13 July 2023; Received in revised form 08 August 2023; Accepted 21 August 2023; Available online 05 October 2023
2412-0758/University of Technology-Iraq, Baghdad, Iraq
This is an open access article under the CC BY 4.0 license http://creativecommons.org/licenses/by/4.0

rotors of various diameters in wind turbines. This method was first developed by Richard Eppler for comprehending the 2D viscous flow around any airfoil. Most airfoil families created using this process have successfully produced wind turbine blades for commercial use [5,6]. Because of their resilience to roughness, greater lift-to-drag ratios, and ability to use a larger swept area for the same size generator in stall-regulated rotors, these airfoils on wind turbines increase the output energy. Depending on the blade length, the NREL airfoils family can generate wind turbines ranging in size from 2kW to 1MW.

In recent years, specialized airfoils have been strongly emphasized, notably thick airfoils used in the midsection of rotor blades. Thick airfoils are desirable because they serve to reduce rotor blade costs by giving more structural strength and rigidity, which aids in lowering the chord of the blade. The airfoil is a critical component of a blade, and its thickness determines its shape. As a result, the parameters of the airfoil substantially impact the blade's characteristics. It is worth noting that the thick airfoils discussed in this work are classified as mid-span wind turbine airfoils that are currently used in many multi-MW horizontal-axis wind turbines (HAWTs) [1].

The shape of the blade is used to classify it regionally, which is important for both aerodynamic and structural concerns [7]. The inherent requirement for larger blades has prioritized developing wind turbine airfoils. Thicker airfoils, which give superior performance to conventional aircraft airfoils, have been examined as a significant option to achieve the competing objectives of structural integrity, geometrical compatibility, and aerodynamic efficiency [7]. Yet, research indicates that increasing the relative thickness of the airfoil along the camber line can reduce its aerodynamic performance [8].

Many techniques have been implemented to optimize the aerodynamics of the airfoils. For example, the inverse design method is a methodology that focuses on regulating velocity or pressure coefficient distributions near a scaled airfoil to construct an airfoil with the best performance and has been widely used [9,10]. The designer's experience and the utilization of tested airfoil families, such as the NREL S-series airfoil families and the DU airfoil series [11-13], are required for this technique to succeed. Wind turbine blades constructed utilizing this method and certain airfoil families have more than 21% relative thicknesses, resulting in high-performing designs with reduced utilized blade material and weight load [1].

Besides the inverse design method, The Institute of Engineering ThermoPhysicss (IET) produced a model based on the RFOIL algorithm [14] and a new 45% root airfoil family with competitive lift performance at high angles of attack when compared to the DU 00-W2-401 (40% relative thickness) [15].

Developing a design for thick airfoils to be employed in the mid-span of a blade requires a difficult balancing act between numerous aerodynamic and structural performance objectives. To overcome this, researchers used numerical optimization, a methodology for developing airfoils with larger purposes. Researchers have improved airfoils' aerodynamic efficiency and structural strength by integrating computational fluid dynamics (CFD) and optimization approaches [16-18]. Despite the significant progress in airfoil design and the productive employment of S-series airfoils, an observable research lacuna exists regarding a comprehensive analysis of various S-series airfoils, particularly concerning their aerodynamic performance and wake behavior at a chord-based Reynolds number of 1×10^6, encompassing a wide range of angles of attack. Addressing this research deficit, the present study embarks upon an exhaustive investigation of four distinct S-series airfoils (S809, S811, S814, and S818) using the commercial Ansys-Fluent Software.

The research distinctly focuses on comparing airfoils that exhibit close morphological resemblance but have slight deviations in the lower front part of the airfoil. This minute variation and its consequential effect on aerodynamic performance form the crux of this study. The future implications of this research lie in the potential use of sophisticated methodologies to modify the lower front shape using smart designs, thereby tailoring the performance according to the associated influencing factors. Through a detailed examination of the aerodynamic performance and the near wake region's characteristics via pressure distribution, lift and drag coefficients, velocity contours, and turbulence kinetic energy.

Being the first to undertake such an in-depth comparative analysis of these specific S-series airfoils under prescribed conditions, this groundbreaking study will contribute significantly to the body of knowledge in airfoil selection. Furthermore, it will lay the foundation for the design of wind turbine blades that are not only more efficient but also more cost-effective. Thus, our research fills a critical gap in understanding S-series airfoils and their performance. It is a valuable reference point for future research and developments in wind energy technology.

2. Test models

The present study investigated the aerodynamics of four different S-series airfoil profiles. The investigated airfoils are: S809, S811, S814, and S818. The airfoils' (x,y) coordinates were obtained from [6]. The airfoils have a cord length of 250 mm with corresponding Reynolds number of 1×10^6. The investigated airfoil profiles are illustrated in Figure 1.

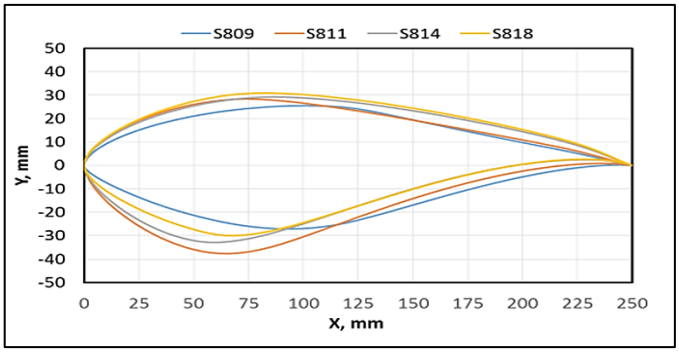

Figure 1: Airfoil sections used in the present work

3. Numerical methodology

3.1 Boundary conditions and mesh generation

Ansys-Fluent commercial software was utilized to solve steady Reynolds averaged Navier-Stokes equations (RANS) for flow around a 2D airfoil domain. The following assumptions were considered in the current work: steady, incompressible, and 2D flow. Because the flow nature around the airfoil is not completely turbulent, the SST-Kω turbulence model, which consists of four equations, was selected as the turbulence model in the current simulations. In addition, the coupled scheme was used in terms of the coupling between pressure and velocity. Finally, a second-order upwind scheme was employed for both the pressure and the momentum. To ensure good convergence for the solved equations, the under-relaxation factor was chosen to be $1x10^{-6}$. Table 1 shows the main parameters set up in the current simulations.

The governing Equations used in the investigation are as follows:

1) The continuity equation was calculated using a steady-state approach.

$$\frac{\partial(\rho U_j)}{\partial x_j} = 0 \tag{1}$$

2) Time – averaged momentum

$$\frac{\partial(\rho U_j U_i)}{\partial x_j} = -\frac{\partial P}{\partial x_i} + \frac{\partial}{\partial x_j}\left[\mu\left(\frac{\partial U_i}{\partial x_j} + \frac{\partial U_j}{\partial x_i}\right) - \overline{\rho u'_i u'_j}\right] \tag{2}$$

3) The k-ω Shear Stress Transport (SST) turbulence model

a. The turbulent kinetic energy, k:

$$\frac{\partial}{\partial t}(\rho k) + \frac{\partial}{\partial x_i}(\rho k U_i) = \frac{\partial}{\partial x_j}\left[(\mu + \sigma_k \mu_t)\frac{\partial k}{\partial x_j}\right] + G_k - \beta\rho\omega + S_k \tag{3}$$

b. The specific dissipation, ω:

$$\frac{\partial}{\partial t}(\rho\omega) + \frac{\partial}{\partial x_i}(\rho\omega U_i) = \frac{\partial}{\partial x_j}\left[(\mu + \sigma_\omega \mu_t)\frac{\partial \omega}{\partial x_j}\right] + \frac{\alpha}{\sigma_\omega{}^2}\left(\frac{\rho}{G_k}\right) - \beta\rho\omega^2 + S_\omega \tag{4}$$

where: ρ : is the density, U: is the velocity vector, μ: is the molecular viscosity, μt: is the turbulent viscosity, Gk: represents the generation of turbulence kinetic energy due to mean velocity gradients, $Sk\ S\omega$: are user-defined source terms, α , β , σk , $\sigma\omega$: are model constants.

Table 1: Parameters setup in the current work

Parameter	Type
Pressure and velocity coupling	Coupled scheme
Turbulence model	SST-Kω
Momentum	Second order upwind
pressure	Second order upwind

The flow domain around the airfoil was discretized

Using a structured "C" type two-dimensional grid. A distance of (20C) extended the grid from the airfoil's leading edge to the domain entrance, (20C) above and below the airfoil, and (40C) from the airfoil's trailing edge to the domain end to avoid reversed/backflow. The velocity inlet and pressure outlet were chosen as the boundary conditions at the domain's entrance and end, respectively. A non-slip wall was also chosen on the suction and pressure sides of the airfoil, as well as along the channel borders. Figure 2 depicts the domain around the airfoil with the zone near the airfoil zoomed in. Table 2 illustrates the boundary condition used in the current simulations.

A Mesh Independence study was carried out to ensure a mesh with high quality for all the simulations in the present work. A structured mesh with an inflation region of 150 layers was built near the airfoil surface to capture the behavior of the boundary layer in this important region. The height of the first layer was carefully chosen to ensure that the first cell's dimensionless height is y+ < 1 to avoid any wall functions. Figure 3 shows the average y+ values at different angles of attack for the examined airfoils in the present work. It can be noticed that all the tested cases have an average y+ of less than 1 near the airfoil surfaces.

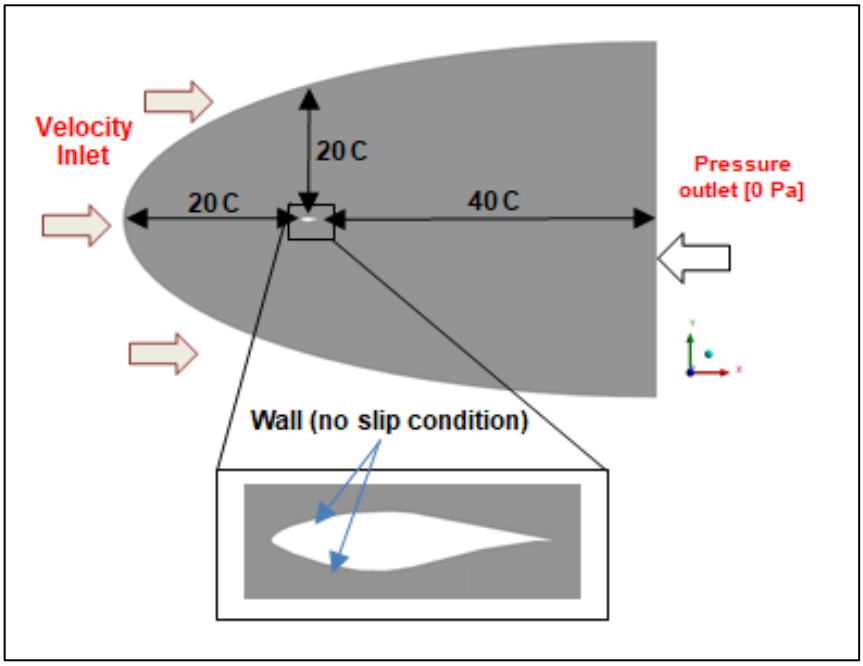

Figure 2: Flow domain around the airfoil

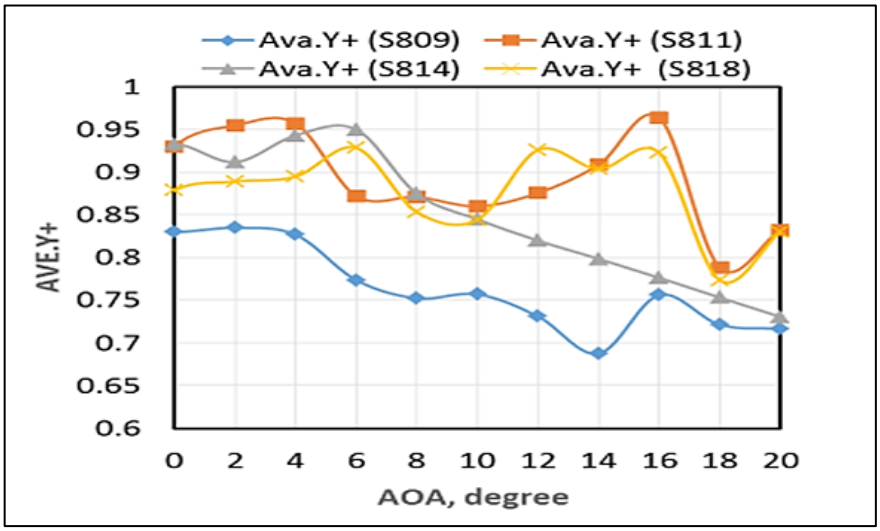

Figure 3: Average y+ at different angles of attack for different airfoil profiles

Table 2: Boundary conditions in the present work

Region	Boundary Type
Entrance	Velocity Inlet [62.466 m/sec]
Exit	Pressure outlet [0 Pa]
Airfoil upper surface	Wall (no-slip condition)
Airfoil lower surface	Wall (no-slip condition)

For the mesh-checking study, lift (Cl) and drag (Cd) coefficients were used as comparative parameters. Seven different meshes were investigated in this study. Figure 4 (a,b) depicts how (Cl) and (Cd) values vary with the number of elements. It can be seen that (Cl) and cd values became mesh independent when the number of elements approached 750500, as shown in Figure 5. As a result, this number of elements was chosen for the remaining simulations.

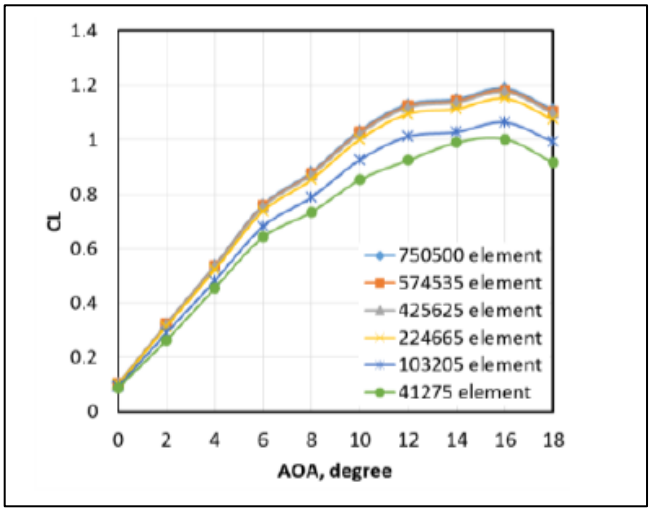

(a)

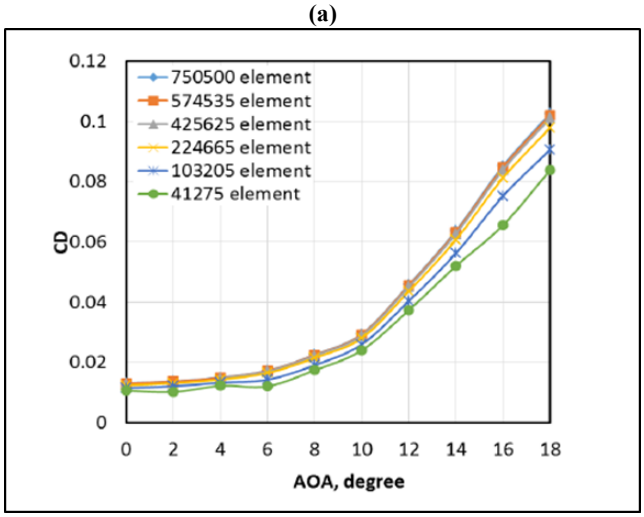

(b)

Figure 4: Mesh independence study for a) lift coefficient (CL) and b) drag coefficient (CD)

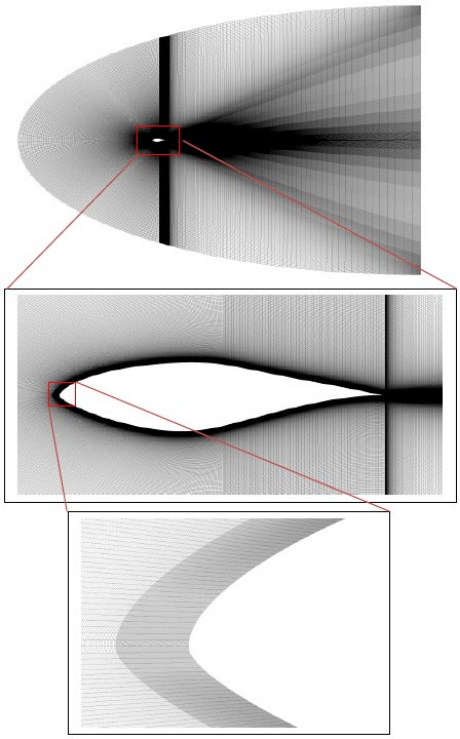

Figure 5: Meshed domain with zoomed leading edge regionarrangement

3.2 Model validation

To affirm the validity of the simulation outcomes obtained in the present study, a comprehensive comparative study has been undertaken, juxtaposing our obtained lift and drag coefficients with experimental data, as reported in the work of [19]. The results of this comparison are graphically illustrated in Figure 6 (a,b).

Figure 6 (a) showcases the comparative analysis of lift coefficients resulting from the current simulation study and those documented by Somer [19], considered across a broad range of angles of attack. An in-depth examination of these outcomes reveals a slight divergence between the numerical simulations and the experimental findings at lower angles of attack. This discrepancy becomes more pronounced at angles exceeding 8°, where the lift coefficient values exhibit substantial divergence from the experimental observations, with this deviation being particularly acute at the maximum tested angle of 18°.

Regarding the lift coefficient, the highest percentage deviation, indicative of overestimation, is found at an angle of attack of 18 degrees, with a deviation of 14.39%. Conversely, the least percentage deviation is discernible at an angle of attack of 8 degrees, featuring a deviation of 5.1%. The mean percentage deviation, derived from the cumulative sum of all positive deviations divided by the total quantity of data points, is approximately 8.68%.

Figure 6 (b) presents a side-by-side examination of the drag coefficient values from the current simulation and the results presented in [20]. The results suggest a commendable fidelity of the current simulation to the experimental data, particularly noticeable at lower angles of attack. However, with an increase in the angle of attack, a distinct deviation from the experimental results becomes apparent, especially at high angles of attack.

About the drag coefficient, the most significant positive percentage deviation appears at an angle of attack of 6°, showing a deviation of 36.91%. On the other hand, the least positive deviation is detectable at an angle of attack of 14°, revealing a deviation of 2.6%. The average positive percentage deviation in drag coefficients, computed from the dataset, is around 18.98%.

The divergence between the numerical simulations and experimental data could primarily be ascribed to the assumptions inherent in the turbulence model, which presumes the flow is fully turbulent. Yet, in actual conditions, the flow transitions from a laminar state to a turbulent one beyond a certain distance from the leading edge. Additionally, the surface conditions could contribute to these observed discrepancies. The ramifications of these findings highlight the necessity for continued investigations to enhance our understanding of these phenomena and improve the predictive accuracy of the simulation model.Besides lift and drag coefficients, the pressure coefficient distribution for the S809 airfoil was also compared with those provided by Feng et al. [20] using the same conditions. The current simulation results showed a good agreement between the results, as seen in Figure 7.

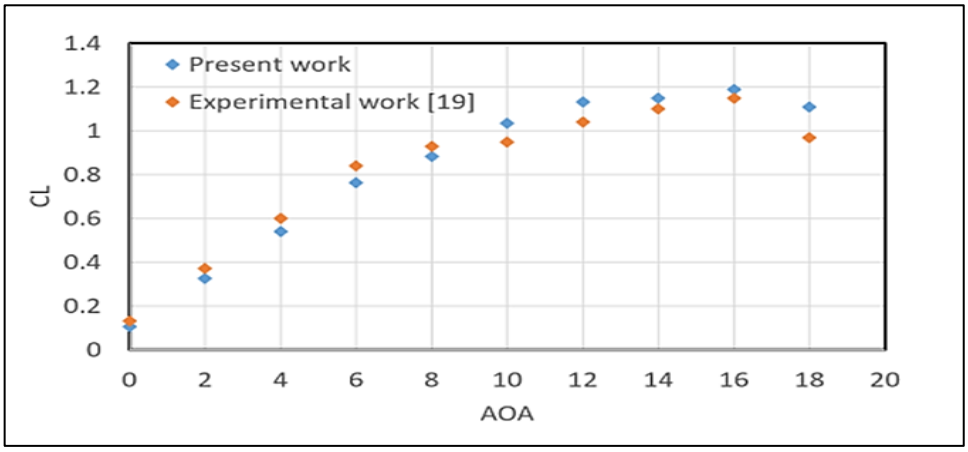

(a)

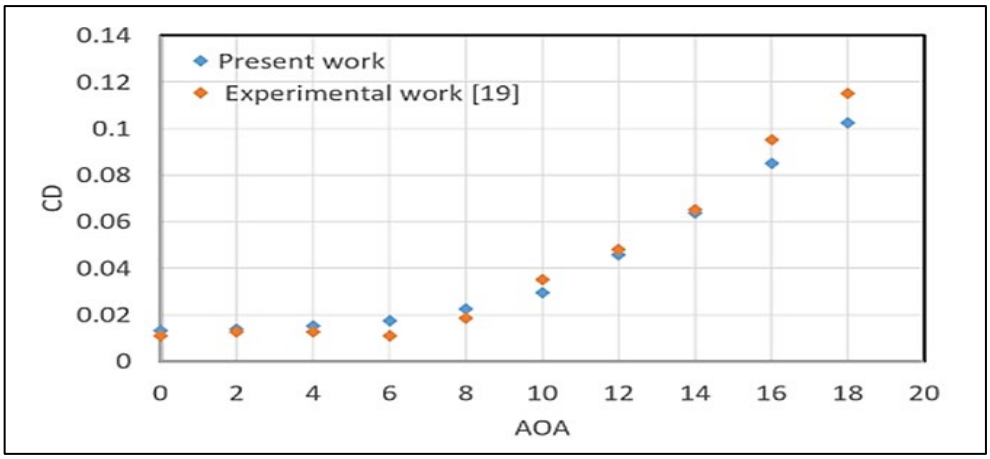

(b)

Figure 6: A comparison of a) Lift coefficient and b) Drag coefficient with experimental data reported in [19]

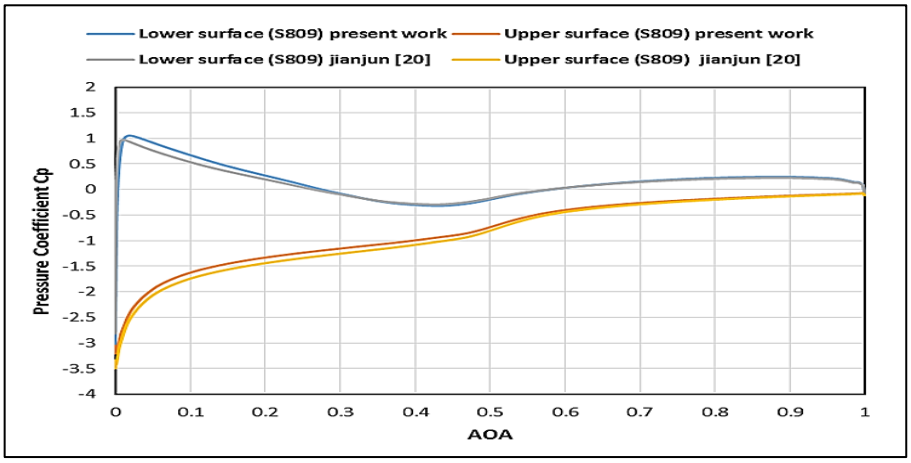

Figure 7: Pressure coefficient comparison with data reported in for the S809 airfoil [20]

4. Results and discussion

4.1 Velocity and turbulence kinetic energy contours

Figure 8 illustrates the velocity contours at an angle of attack 10° for the airfoils S809, S811, S814, and S818. The contours clearly show that the flow velocity on the upper surface of the tested airfoil was higher than that on the lower surface. This means the pressure on the upper surface is lower than on the lower surface. In addition, the flow separates from the upper surface of the airfoils near the trailing edge, where a region of recirculated flow occurs near the end of the airfoil's upper surface. The recirculation region on the upper surface of S809 is larger than the other tested airfoils. In addition, at a higher angle of attack, 16° the velocity contours clearly showed that flow completely separated from the upper surface of the S809 and S814 airfoils. This was previously seen in the pressure distribution and lifted variation with the angle of attack. On the other hand, for both S811 and S818 airfoils, the velocity contours show that flow remains attached, as shown in Figure 9.

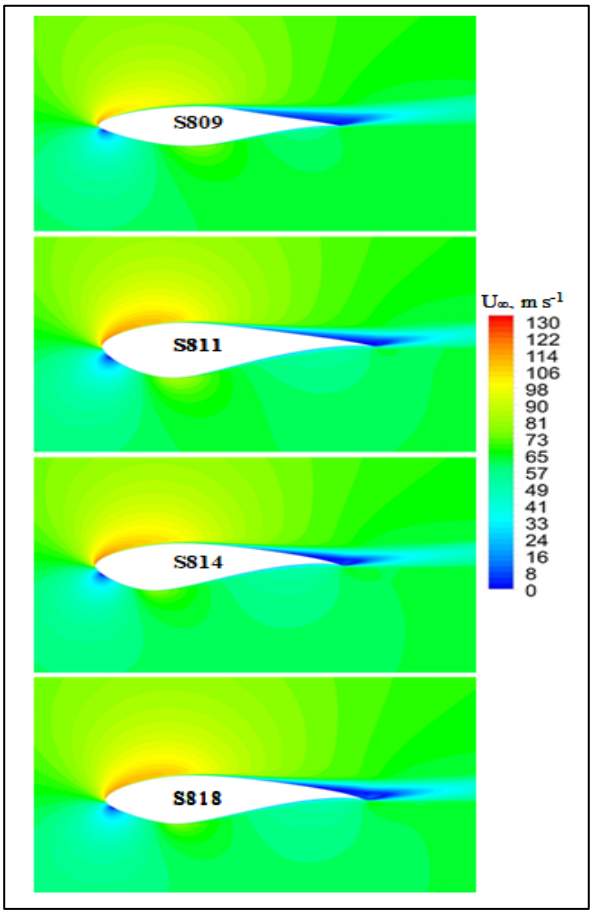

Figure 8: Velocity contours for S809, S811, S814, and S818 airfoils at angle of attack 16°

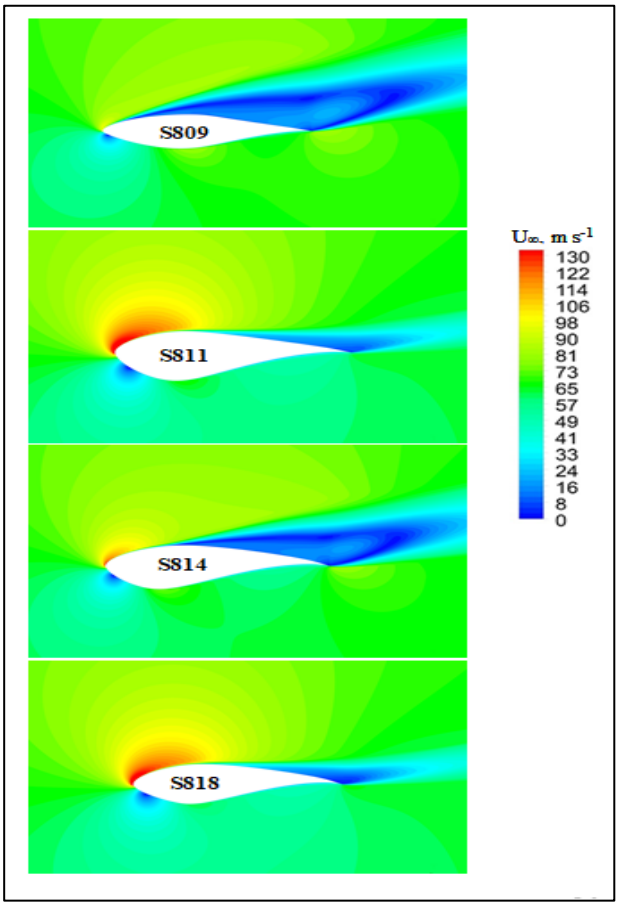

Figure 9: Turbulence kinetic energy contours for S809, S811,S814, and S818 airfoils at angle of attack 10°

Moreover, to understand the effect of the profile change of the airfoils on the wake region behind the airfoil, the turbulence kinetic energy contours were also drawn at angles of attack 10° and 16°. Figure 10 shows the turbulence kinetic energy for each airfoil at the angle of attack 10°. It can be seen that S811 has the lowest turbulence kinetic energy among the tested airfoils. In addition, airfoils S818 and S814 have the highest near-wake turbulence kinetic energy.

However, at higher angles of attack 16°, Figure 11 shows that the turbulence kinetic energy near the surface of the S809 and S814 airfoils is the highest compared to the S811 and S818 airfoils. This high level of turbulence kinetic energy was due to the severe separation near the surface of the former airfoils at this angle of attack.

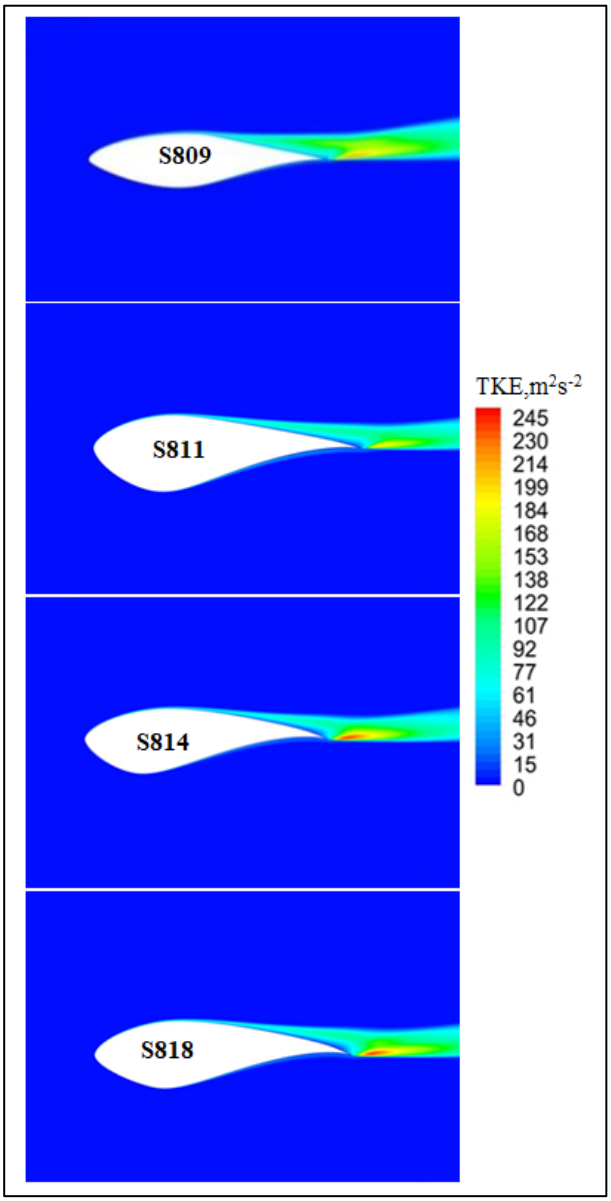

Figure 10: Turbulence kinetic energy contours for S809, S811, S814, and S818 airfoils at angle of attack 10°

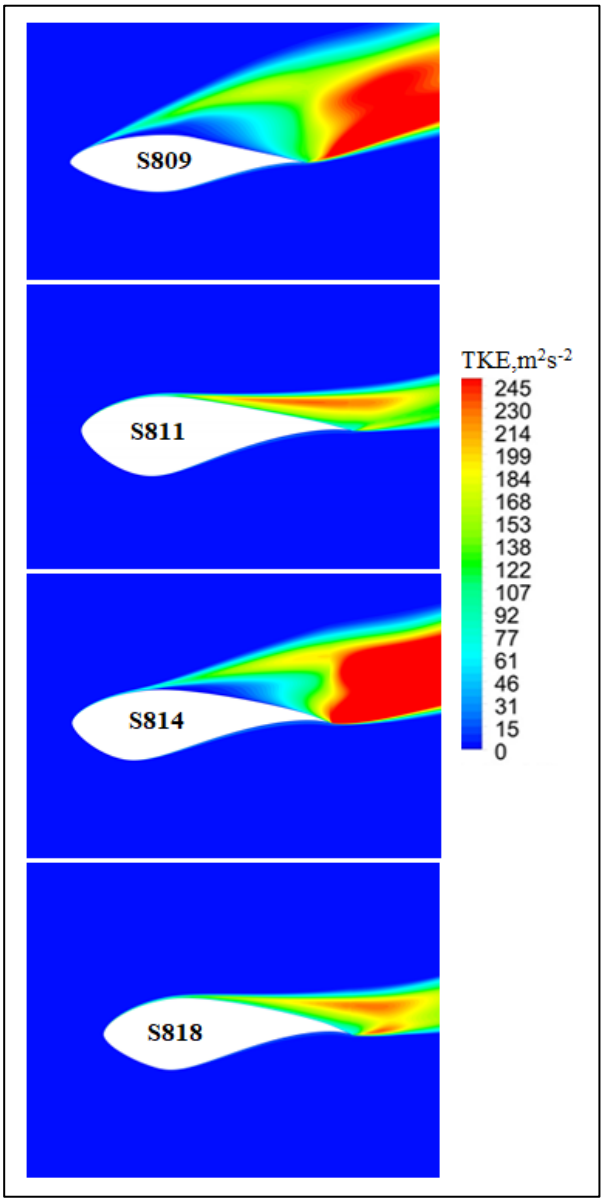

Figure 11: Turbulence kinetic energy contours for S809, S811, S814, and S818 airfoils at angle of attack 16°

4.2 Lift and drag coefficients

This section discusses the influence of airfoil profiles S809, S811, S814, and S818 on aerodynamic properties, lift and drag. Figure 12 illustrates the lift coefficient for the four airfoils at different angles of attack. It can be seen that the S809 airfoil produced the lowest maximum lift coefficients of 1.25 at a critical angle of attack 12° The smallest critical angle of attack of 10° was recorded for the airfoil. This means that the S814 airfoil stalls earlier than the other tested airfoils. In addition, the highest maximum lift coefficient was achieved with airfoils S811 and S818 with the critical angle of attack of 16°.

Further to the lift coefficient, the drag coefficient was also plotted against varying angles of attack, as depicted in Figure 13. An examination of the plot reveals a noteworthy trend; all the tested airfoils exhibit identical drag coefficient values across the range of angles of attack between zero and 10 degrees. However, the behavior of the airfoils starts to differentiate beyond an angle of attack of 10 degrees.

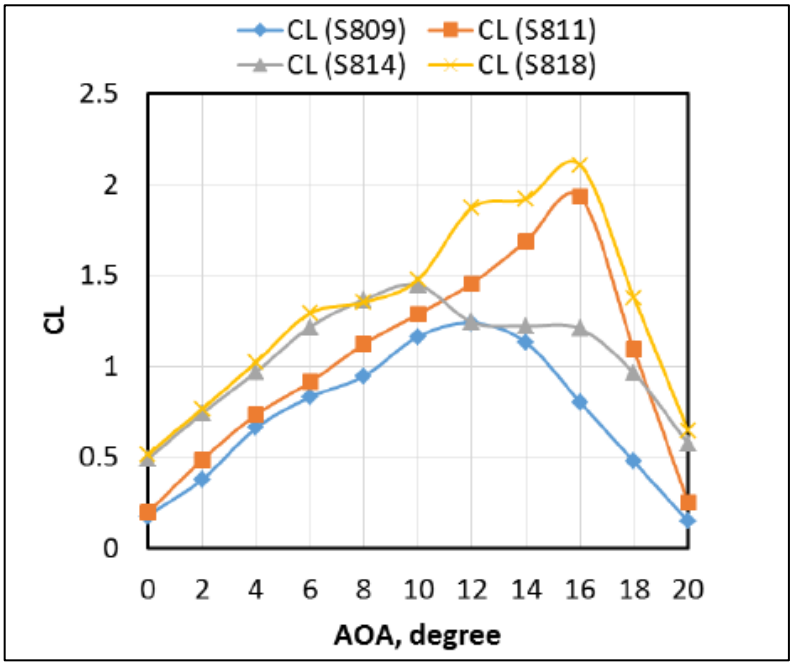

Figure 12: Lift coefficient for S809, S811, S814, and S818 airfoils at different angles of attack

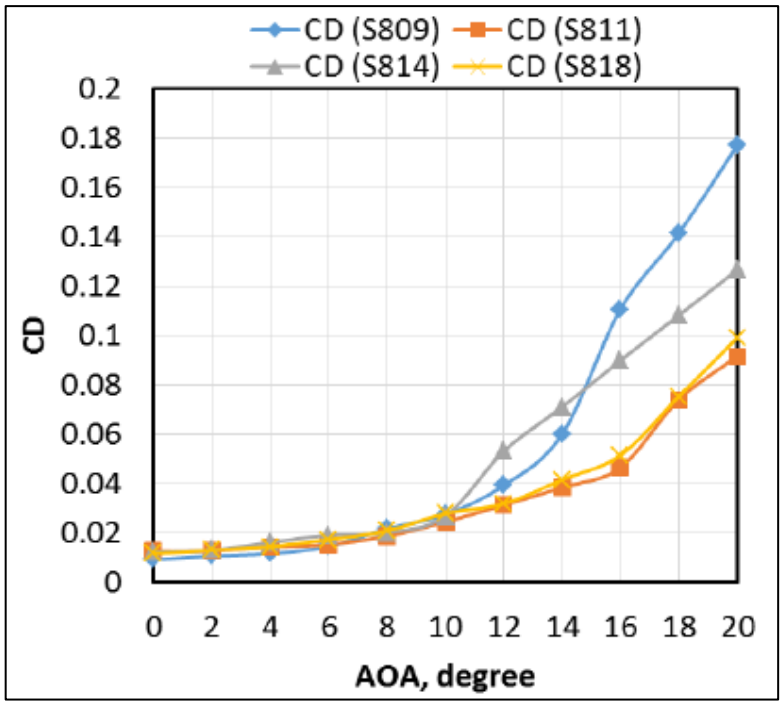

Figure 13: Drag coefficient for S809, S811, S814, and S818 airfoils at different angles of attack

Particularly, the S809 and S814 airfoils manifested the greatest drag at the stall angle of attack compared to their S811 and S818. This outcome suggests a smoother flow separation than the S809 and S814 airfoils compared to the S811 and S818 airfoils.This variation in drag behavior at larger angles of attack, particularly during stall conditions, can be attributed to the distinct geometric profiles and consequent flow characteristics of these airfoil designs. The resultant smoother separation on the S811 and S818 airfoils suggests a more delayed stall characteristic, which can significantly impact the aerodynamic performance and efficiency of the wind turbine blades they are employed. These insights underline the critical role that airfoil design plays in achieving optimal wind turbine performance. Moreover, the lift-to-drag ratio was drawn to better understand each airfoil's aerodynamic performance, as seen in Figure 14.

Figure 14 shows that the best performance, the highest lift drag ratio, is achieved using the S818 airfoil at a wide range of angles of attack compared to the other tested airfoils.

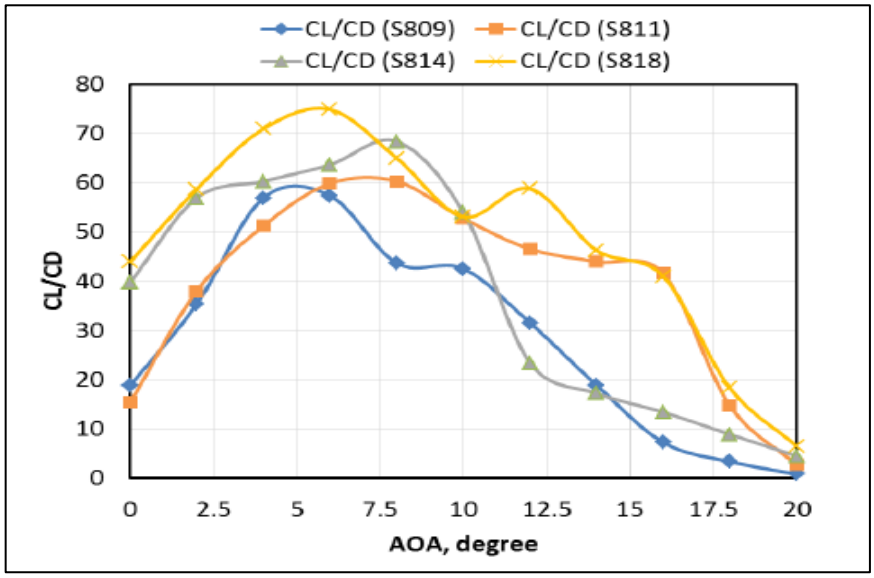

Figure 14: Lift-to-drag ratio for S809, S811, S814, and S818 airfoils at different angles of attack

4.3 Pressure coefficients

The preceding section articulated the implications of airfoil shape on lift generation. This segment pivots to assessing the repercussions of airfoil shape on the distribution of pressure, centering on angles of attack at 10° and 16°, depicted in Figures 15 and 16, respectively.

Upon evaluating an angle of attack at 10° the influence of airfoil profile shape on the pressure coefficient across the airfoil surface is illuminated in Figure 15. The analysis reveals that the pressure on the upper surface of the S809 airfoil is the lowest among the examined profiles for the segment extending from the leading edge halfway through the airfoil chord length. As for the other airfoils, namely S811, S814, and S818, a slight elevation is noticeable approximately at the quarter-chord position.

Although this elevation might intuitively suggest the presence of a small separation bubble and subsequent turbulent reattachment, it is crucial to clarify that determining the exact location of flow separation or the existence of a separation bubble from pressure coefficient plots alone can be misleading. Instead, accurate conclusions require more comprehensive investigation techniques, such as Wall shear stress distribution.When considering the correlation between pressure distribution and lift force, the convention that the area beneath the pressure curve symbolizes the lift force stands. Here, the area under the pressure curve for the S818 airfoil is notably larger than for the other tested airfoils, corroborating the lift coefficient patterns previously observed in Figure 12.

Figure 16 depicts the pressure distribution at an elevated angle of attack of 16°. Upon examination of Figure 16, it is observable that in the vicinity of the leading edge of the examined airfoils, the suction pressure near the leading edge of the S818 and S811 models significantly overshadows that of the other tested airfoils, S809 and S814. Interestingly, the suction pressure near the leading edge of the S809 model falls below that of the S814 airfoil.Furthermore, the area beneath the pressure curve of the S809 and S814 models falls short compared to that of the S818 and S811, implying that the lift generated by the latter airfoils surpasses that produced by the other models. It is important to note that inferring stalling based solely on a constant pressure distribution is typically inappropriate. However, almost constant pressure on the upper and lower surfaces of S809 and S814 after a quarter of the airfoil chord length does suggest that these airfoils may be operating beyond their critical angle of attack.

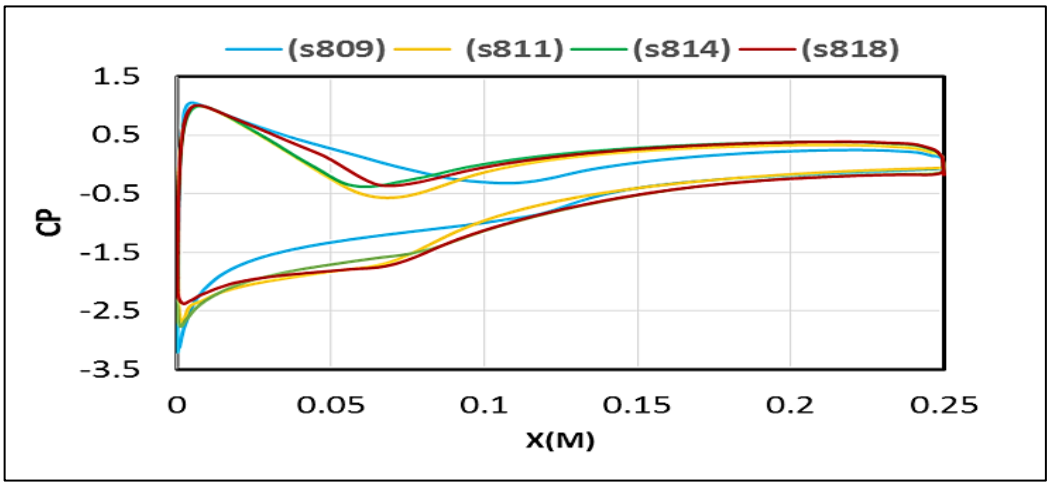

Figure 15: Pressure coefficient distribution for S809, S811, S814, and S818 airfoils at angle of attack 10°

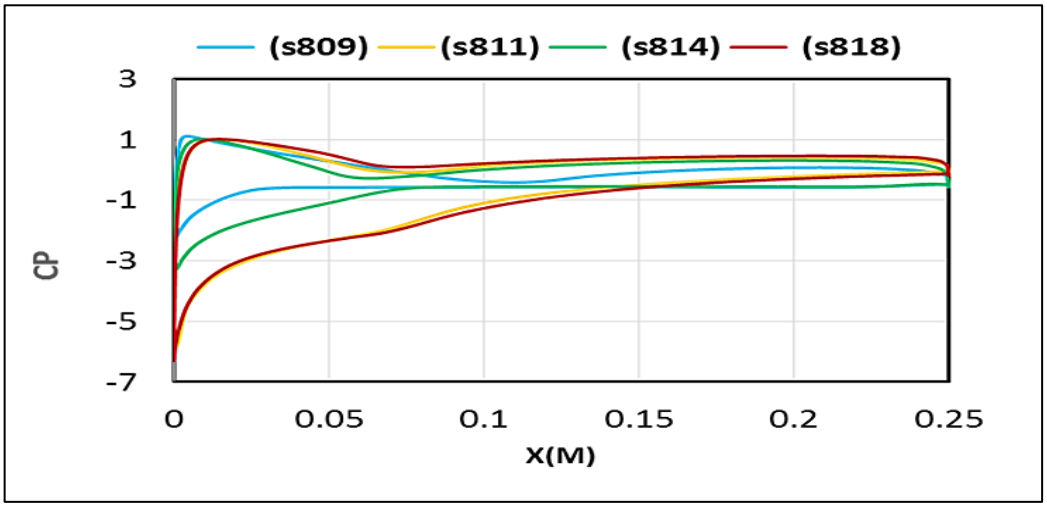

Figure 16: Pressure coefficient distribution for S809, S811, S814, and S818 airfoils at angle of attack 16°

This insight aligns with observations made in Figure 12, wherein both the S809 and S814 airfoils appear to stall at an angle of attack exceeding 10°, representing the critical angle at which the maximum lift coefficient was accomplished. On the other hand, the airfoils S811 and S818 demonstrate a more expansive area beneath the pressure curve, signifying continued lift production at this elevated angle of attack.Despite this, the pressure distribution becomes nearly constant after one-third of the chord length, a characteristic that hints at the airfoils' stalling behavior. This was also reflected in Figure 12, where it was observed that these airfoils stalled post reaching an angle of attack of 16°. However, while these patterns may suggest stalling behavior, definitive confirmation would necessitate corroborative evidence, such as drag data, as shown in Figure 13, or wall shear stress results, which can more definitively indicate flow separation or stalling.

4.4 Wall shear stress distribution

This section shows the wall shear stress distribution on the upper side of the four tested airfoils along the chord length at two angles of attack, 10° and 16°, as shown in Figures 17 and 18, respectively.

From Figure 17, at the angle of attack of 10º, it can be seen that wall shear stress distribution on the upper side of all tested airfoils started at a high value near the leading edge of the airfoils. This is because flow accelerates near the airfoil's leading edge on the suction side. After this high shear stress peak, the shear stress started to sharply down for the airfoils S811, S814, and S818 until it reached a certain distance from the leading edge of the airfoils at about 25% C, where it started to drop again but in a smoother manner than near the leading edge region. However, for airfoil S809, after the peak value of the shear stress curve, the shear stress dropped more than the other tested airfoils until about 35% C, where the shear stress values for the airfoil, as mentioned earlier, started to drop further. As shear stress is directly linked to the boundary layer on the surface of any solid surface, this behavior of the flow indicates a possible transition in the boundary layer on the airfoils.

Moreover, at an angle of attack of 16°, from Figure 18, it can be noticed that the shear stress on both S809 and S814 airfoils dropped from the peak value of the shear stress to zero. At zero shear stress points, the flow on the upper surface of the S809 and S814 separates at this angle of attack. In addition, one can notice that the point where the flow separated from S809 airfoil occurs at a smaller distance compared to S814. Moreover, the flow remained separated until the trailing edge of the airfoils. However, the shear stress on the surface of the S811 and S818 did not go to zero value. As a result, the flow remained attached to the upper surface of the airfoils, as mentioned earlier. This was previously confirmed in Figure 12 and Figure 16, where both airfoils did not stall at this angle of attack.

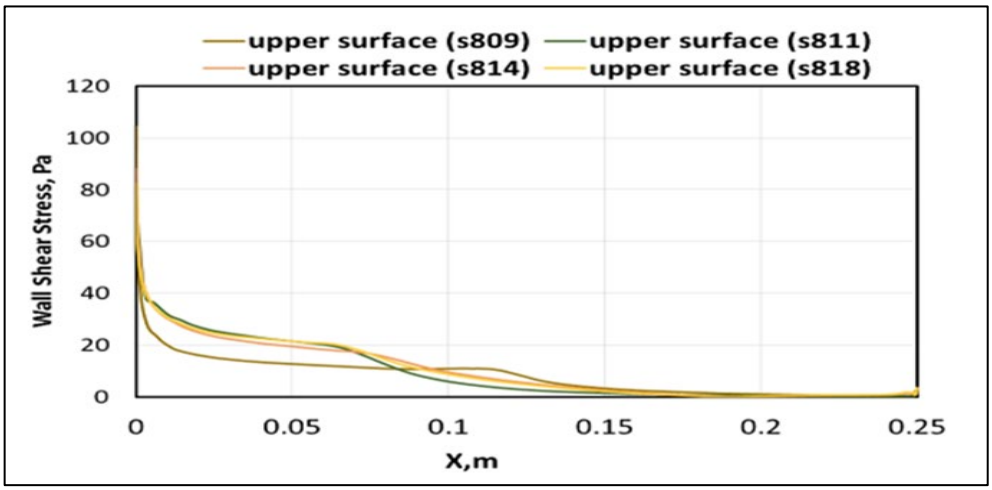

Figure 17: Wall shear stress distribution S809, S811, S814, and S818 airfoils at angle of attack 10°

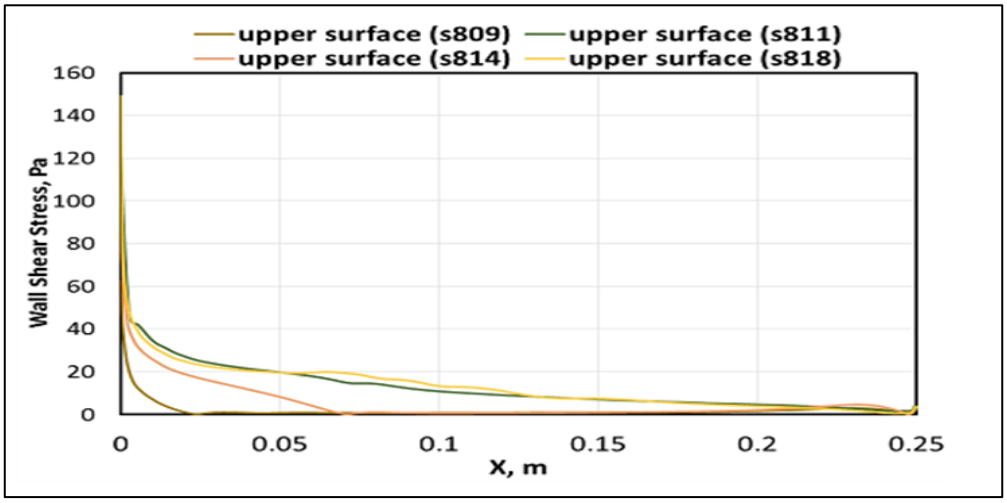

Figure 18: Wall shear stress distribution S809, S811, S814, and S818 airfoils at angle of attack 16°

5. Conclusion

The objective of this research was to numerically explore the influence of varying thick airfoil profiles on the aerodynamic characteristics and turbulence behavior in the near wake region at a Reynolds number of $Re = 1\times10^6$ and across an extensive range of angles of attack. The airfoil profiles scrutinized included the S809, S811, S814, and S818, with the angles of attack extending from 0° to 20°.

Our investigation revealed superior performance from the S811 and S818 airfoils compared to the S809 and S814 counterparts. The heightened lift coefficients for S811 and S818 can be attributed to their distinctive front edge and lower surface geometry. Further, these airfoils exhibited diminished drag at high angles of attack (> 16°) and achieved a notable drag reduction within the 10° to 16° range. These findings underscore the efficacy of the S811 and S818 airfoils in enhancing overall aerodynamic performance.

The flow domain in the vicinity of the airfoil surface and the turbulence kinetic energy were examined to confirm the aerodynamic characteristics. At an angle of attack of 16°, clear flow separation on the upper surfaces of S809 and S814 was evident in the velocity contours. The turbulence kinetic energy distributions corroborated this observation, depicting high turbulence levels around the airfoils due to severe flow separation at this angle of attack. This contrasted markedly with the S811 and S818 airfoils, which showed considerably reduced turbulence kinetic energy in the near-wake zone.

These findings suggest that thicker airfoils like the S811 and S818 for wind turbine blade design would ideally be positioned towards the blade's root, where high lift and low drag are critical for structural balance and efficient power generation.

In summary, the judicious selection of airfoil profiles, particularly those akin to S811 and S818, can ameliorate aerodynamic performance and decrease turbulence kinetic energy in the near wake region. This research provides critical insights for designing and optimizing high-performance airfoils for wind energy and other relevant applications.

Author contributions

Conceptualization, H. Jaffar, L. Al-Sadawi, A. Khudhair and T. Biedermann; methodology, H. Jaffar; software, H. Jaffar, L. Al-Sadawi, A. Khudhair and T. Biedermann; validation, H. Jaffar. ;formal analysis, H. Jaffar; investigation, H. Jaffar, L. Al-Sadawi and A. Khudhair; data curation, H. Jaffar; writing—original draft preparation, Ha. Jaffar; writing—review and editing, H. Jaffar; visualization, H. Jaffar; supervision, L. Al-Sadawi, A. Khudhair and T. Biedermann.; project administration L. Al-Sadawi, and A. Khudhair;. All authors have read and agreed to the published version of the manuscript.

Funding

This research received no specific grant from any funding agency in the public, commercial, or not-for-profit sectors.

Data availability statement

The data that support the findings of this study are available on request from the corresponding author.

Conflicts of interest

The authors declare that there is no conflict of interest.

References

[1] Navigant Research, Navigant Research World Market Update 2012 Comments. Web. 08 Nov. 2013.

[2] Burton, T., Wind energy handbook, Chichester, West Sussex, Wiley, 2011.

[3] M. R. Ahmed, Blade sections for wind turbine and tidal current turbine applications-current status and future challenges, Int. J. Energy Res., 36 (2012) 829-844. https://doi.org/10.1002/er.2912

[4] Tangler, J. L., Somers, D. M., United States., National Renewable Energy Laboratory (U.S.), & Airfoils Incorporated. NREL airfoil families for HAWTs. Golden, Colo: National Renewable Energy Laboratory, (1995).

[5] T. Winnemöller and C. P. Van Dam, Design and numerical optimization of thick airfoils including blunt trailing edges, J. Aircr., 44 (2007) 232e40. https://doi.org/10.2514/1.23057

[6] F. Grasso, Development of thick airfoils for wind turbines, J. Aircraft, 50 (2013) 975. http://dx.doi.org/10.2514/1.C032182

[7] P.Schubel and R. Crossley, Wind turbine blade design review, J. Wind Eng., 36 (2012) 365e88.http://dx.doi.org/10.1260/0309-524X.36.4.365

[8] W. A. Timmer, R. Van Rooy, Thick airfoils for HAWTs, J. Wind Eng. Ind. Aerodyn., 39 (1992) 151e60.https://doi.org/10.1016/0167-6105(92)90541-H

[9] M. S. Selig, M. D. Maughmer, Multipoint inverse airfoil design method based on conformal mapping, AIAA J., 30 (1992)1162e70. https://doi.org/10.2514/3.11046

[10] Drela M. XFOIL, An analysis and design system for low Reynolds number airfoils[M]//Low Reynolds number aerodynamics, Springer Berlin Heidelberg, 1989, 1e12. https://doi.org/10.1007/978-3-642-84010-4_1

[11] Tangler J. L. and Somers D. M., NREL airfoil families for HAWTs[M]. National Renewable Energy Laboratory; 1995.

[12] W. A. Timmer and R. Van Rooij, Summary of the Delft University wind turbine dedicated airfoils, J. Sol. Energy Eng., 125 (2003) 488e96.https://doi.org/10.1115/1.1626129

[13] R. Van Rooij and W. A. Timmer, Roughness sensitivity considerations for thick rotor blade airfoils, J. Sol. energy Eng. 125 (2003) 468e78.https://doi.org/10.1115/1.1624614

[14] Van Rooij R., Modification of the boundary layer calculation in RFOIL for improved airfoil stall prediction, Report IW-96087R. The Netherlands, TUDelft, 1996.

[15] X. Li, K. Yang, L. Zhang,J. Bai and J. Xu, Large thickness airfoils with high lift in the operating range of angle of attack, J. Renew. Sustain Energy, 6 (2014) 033110.https://doi.org/10.1063/1.4878846

[16] P. Fuglsang and C. Bak, Development of the Risø wind turbine airfoils, Wind Energy, 7 (2004) 145e62.http://dx.doi.org/10.1002/we.117

[17] Tangler, J. L., Somers, D. M., United States., National Renewable Energy Laboratory (U.S.), & Airfoils Incorporated, NREL airfoil families for HAWTs. Golden, Colo: National Renewable Energy Laboratory, 1995.

[18] Wind Turbine Airfoils, Web. 23 Nov. 2013. http://wind.nrel.gov/airfoils/

[19] Somers D., Design and experimental results for the S809 airfoil, NREL/SR-440-6918. Tech. Rep. NREL, 1997

[20] J. Feng, Y. Lin, G. Zhu, and X. Luo, Effect of synthetic jet parameters on flow control of an aerofoil at high Reynolds number, Sādhanā, 44 (2019) 1-10. https://doi.org/10.1007/s12046-019-1173-2